# Designing the 3D-microbattery geometry using the level-set method

Vahur Zadin [a],[*], Daniel Brandell [b], Heiki Kasemägi [a], Jaan Lellep [c], Alvo Aabloo [a]

[a] Intelligent Materials and Systems Lab, Institute of Technology, Tartu University, Nooruse 1, 50411 Tartu, Estonia
[b] Department of Chemistry — Ångström, Uppsala University, Box 538, 75121 Uppsala, Sweden
[c] Institute of Mathematics, Tartu University, Liivi 2, 50409 Tartu, Estonia

## HIGHLIGHTS

► Simulations and geometrical optimization of the 3D-microbattery trench geometry.
► Application of the level-set method in an electrochemical system.
► Application of the structural topology optimization in an electrochemical system.
► General method for (3D-micro)battery geometry optimization.
► Power optimization of the 3D-trench geometry.

## ARTICLE INFO

## ABSTRACT

Strategies for automatic design of power-optimized 3D-microbattery geometries are here investigated by utilization of the level-set method with structure topology optimization. The methodology is extended from solid mechanics to electrochemical systems, where battery operation is simulated using the Nernst—Planck equation. The calculations are carried out for the 3D-"trench" geometry with $LiCoO_2$ and $LiC_6$ as electrodes, separated with a $LiPF_6 \cdot PEO_{20}$ polyethylene oxide polymer electrolyte. With the goal to achieve a maximum uniform electrochemical activity over the electrode surface area, an optimized electrode design is produced by coating the current collectors non-uniformly with active material. This is shown to be an effect of the 3D design of the cell. Evaluation of the resulting optimized cell by simulations of the discharge process demonstrates uniform electrode material utilization and almost uniform current density distribution over the entire electrode—electrolyte interface. Comparisons between optimized and non-optimized geometries showed that the geometry optimization increased the cell performance up to 2.25 times. This effect is mainly achieved by minimizing the internal energy losses caused by non-uniformities in the ionic transport in the battery.

## 1. Introduction

Several emerging microtechnology branches, such as micro-electromechanical system (MEMS) devices and small-scale medical devices like e-pills, require portable power supplies of ~1 mm³ dimensions or smaller. Unfortunately, the development of such miniature portable power sources has been outpaced by the microtechnology development, resulting in technical devices which lack appropriate power storage [1]. To fill this gap, small scale high power and energy density batteries, capable of providing both high current and capacity, are needed [1]. Therefore, a new

type of thin-film microbatteries with 3D electrodes — the 3D-microbatteries (3D-MBs) — has been suggested [1—3]. The required combination of high power and energy density is achieved by constructing the electrodes in 3D-arrangements, generating large internal surface areas, high electrode capacities and small battery footprint areas.

The manufacturing of these kinds of electrodes is technically complicated, thereby often resulting in electrodes with non-uniform material coating [3]. At the same time, the very first mathematical simulations of the 3D-MB systems have demonstrated non-uniform current densities in the electrodes and electrolytes [4—6], indicating possible performance losses due to inhomogeneous electrode reactions. It is then likely that these two different non-uniformities co-interact in the battery. Previous simulations [6] have demonstrated how uniformly coated electrodes suffer performance losses since certain parts of the material

* Corresponding author. Tel.: +372 7374834; fax: +372 737 4825.
E-mail address: vahur.zadin@ut.ee (V. Zadin).

are discharged or charged faster than others. This could, to some degree, be adjusted, for example, by using different electrolytes [7].

An optimal 3D-MB performance with respect to both power and energy supply is achieved when the electrochemical activity over the entire electrode surfaces is uniform during battery operation. One way to obtain such a situation would be to utilize electrodes with a non-uniform material layer thickness distribution and fit it to the non-uniformity in the current distribution resulting from the 3D-design. Considering the complexity of the system, advanced optimization methods are needed for such calculations.

Structural optimization methods with compliance minimization from structural mechanics [8] present a suitable approach, since these methods allow a systematical and simultaneous design of the electrode geometry toward its optimal current distribution. However, homogenization methods such as solid isotropic material with penalization (SIMP) [9] can create geometries with large voids which are unsuitable for electrode material deposition. A region-based approach, such as the level set method [10–12] is therefore preferable.

The level set method is often used to solve compliance minimization problems in structural mechanics [11–13], or to model multiphase flow in fluid dynamics [14,15]. Recently, a substantial number of studies applying the level set method for physical problems have been published. Zhuang et al. [16] used the level set method to optimize heat transport problems, while Luo et al. [17] optimized the shape and topology of an electromechanical actuator.

In the current study, the modeling of the 3D-MB in the "trench" geometry [1,3,6] has been carried out using the Nernst–Planck equation [18] and concentrated solution theory [19–24]. The simulations serve two major goals − to understand the ionic transport in the 3D battery system and to optimize the 3D-MB geometry. Therefore, an optimization algorithm utilizing the level-set method is proposed for a 3D-MB, and a suitable objective function for optimization is provided. The 3D-MB geometry is thereafter optimized, and simulations of discharge processes are carried out to compare the optimized and non-optimized cells.

## 2. Materials and methods

### 2.1. The level set method

Generally in the level set method, a moving material boundary is expressed as a zero level set of a higher dimensional function in the design domain. This is schematically illustrated in Fig. 1. The level set function $\phi$ divides the material region into two different materials, so that:

$$\phi(x) > 0, \quad x \in \Omega_1 \quad \text{(region 1)} \tag{1.1}$$

$$\phi(x) = 0, \quad x \in \partial\Omega \quad \text{(region boundary)} \tag{1.2}$$

$$\phi(x) < 0, \quad x \in \Omega_2 \quad \text{(region 2)} \tag{1.3}$$

Then, different regions in the design domain are defined by the Heaviside function:

$$H(\phi) = \begin{cases} 1, & \phi \geq 0 \\ 0, & \phi < 0 \end{cases} \tag{2}$$

For example, the spatial conductivity distribution of the electrode–electrolyte system is expressed as:

$$\sigma(\phi) = \sigma_1 \cdot H(\phi) + \sigma_2 \cdot (1 - H(\phi)), \tag{3}$$
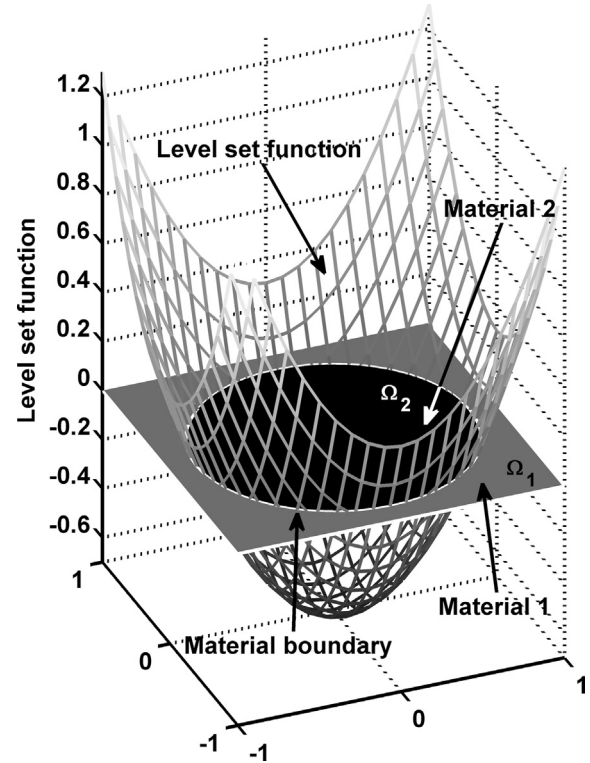


**Fig. 1.** Material properties and geometry regions expressed through the level-set function. The zero level set represents the material boundary and divides the whole region into two subregions with different material properties. When the level set function is modified during the calculation, the material boundary is moved.

where $\sigma_1$ represents the (electronic) conductivity of the electrodes and $\sigma_2$ is the (ionic) conductivity of the electrolyte. In conjunction, these describe the total conductivity distribution in the cell.

To avoid numerical problems at the region interfaces, a smoothed Heaviside function is used during the calculations [11,13]. The boundary of the regions is identified by using the Dirac delta function, defined as $\delta(\phi) = H'(\phi)$ and expressed depending from the level set function:

$$\delta(x) = \frac{\mathrm{d}H}{\mathrm{d}x} = \nabla H \cdot \frac{\nabla\phi}{|\nabla\phi|} = \delta(\phi)|\nabla\phi| \tag{4}$$

The normal vector at the region interfaces is defined as:

$$\vec{n} = \nabla\phi/|\nabla\phi|, \tag{5}$$

Finally, the level set function is a solution of Hamilton Jacoby type equation:

$$\frac{\partial\phi}{\partial t} + V_\mathrm{n}|\nabla\phi| = 0, \tag{6}$$

where $V_\mathrm{n}$ is the normal velocity of the moving boundaries in the system. By solving this equation, it is possible to track the movement of the regions in the design domain.

### 2.2. The objective function

The strategy to optimize the 3D-MB geometry is to reach as uniform electrochemical activity as possible on the electrode surface. While this condition is fulfilled, the lithiation/delithiation of the electrodes is uniform and the battery performance is maximal.

To carry out an optimization procedure, it is necessary to define a function to be minimized (or maximized) − an objective function. Here we consider an objective function based on the current density in the electrolyte, which accounts for the main resistance in the battery cell. The current density is directly correlated to the concentration dependent ionic conductivity, and is a sum of the diffusive and migrative fluxes.

Similarly to the optimization of heat transport [16], we propose an objective function as a functional of the current density, expressed as:

$$F = \int_{\Omega} \sqrt{j_x^2 + j_y^2 + j_z^2} \, d\Omega \qquad (7)$$

The objective function defined in Eq. (7) will be minimized, if the average current density in the cell is as uniform as possible.

### 2.3. General optimization problem

By minimizing the objective function, the most uniform current density distribution in the 3D-MB geometry is achieved. To ensure that the battery electrodes will not fill the whole cell, a constraint is introduced: the battery electrodes sustain a specific volume $V^*$. The constraint is introduced by using the Heaviside function applied to the level-set variable. To minimize the objective function, specified in Eq. (7), the general topology optimization problem for the 3D-MB can then be written as [8]:

$$\text{minimize} \quad F(\phi) = \int_{\Omega} \sqrt{j_x^2 + j_y^2 + j_z^2} \, d\Omega \qquad (8.1)$$

$$\text{subject to} \int_{\Omega} H(\phi) d\Omega = V^* \qquad (8.2)$$

where $V^*$ is the volume of the electrodes and $F$ is the objective function, calculated by a system of partial differential equations presented in paragraph 2.5.

The implementation of the optimization routine follows Wang et al. [11]. Accordingly, the constraints in the optimization are implemented using the method of Lagrange multipliers:

$$J = \int_{\Omega} \left[ F(\phi) + \lambda \left( H(\phi) - \frac{V}{V_{\text{total}}} \right) \right] d\Omega \qquad (9)$$

The speed function is achieved by minimizing Eq. (9), as demonstrated by Wang et al. [11]. Since the mathematical derivation of the final speed function can be found in the literature [11] and it is not an aim of current work, we present here only the final result. The normal velocity of the zero level set of the level set surface can be calculated as $V_n = (F + \lambda)\delta(\phi)$ [11,13]. It is known from structural mechanics that it is sufficient to know the normal velocity of the domain boundary to describe the change of its shape. As a result, by using Eq. (6), the evolution of the electrode boundary toward its optimal shape can be calculated [11,13]:

$$\frac{\partial \phi}{\partial \tau} + (F + \lambda)\delta(\phi)|\phi| = 0, \qquad (10)$$

where $\tau$ is pseudo time, representing the optimization steps. Pseudo time is used instead of time to emphasize that while the shape of the electrodes evolves toward optimal, the mass and current distribution in the cell are at steady state during every optimization step. When solving this optimization problem, the solution will converge toward a local minimum based on the initial value. The solution of the optimization problem is terminated if the following condition is fulfilled [11]:

$$\int |V_n| \delta(\phi) |\nabla \phi| d\Omega \leq \gamma_{\text{tol}} \qquad (11)$$

where $\gamma_{\text{tol}}$ is specified error limit.

To calculate the Lagrange multiplier, the volume of the electrodes must be constant [11]:

$$\frac{\partial}{\partial \tau} \left( \int_{\Omega} H(\phi) d\Omega - V^* \right) = \int_{\Omega} \frac{\partial H(\phi)}{\partial \phi} \frac{\partial \phi}{\partial \tau} d\Omega = \int_{\Omega} \delta(\phi) \frac{\partial \phi}{\partial \tau} d\Omega = 0 \qquad (12)$$

Now, the Lagrange multiplier can be expressed as [11]:

$$\lambda = \frac{\int_{\Omega} F\delta^2(\phi)|\phi| d\Omega}{\int_{\Omega} \delta^2(\phi)|\phi| d\Omega} \qquad (13)$$

### 2.4. Solution of the level set equation

The level set equation is solved in Comsol Multiphysics 4.2 [25] by using the "Level Set toolbox" in the computational fluid dynamics module. The toolbox includes methods for reinitialization and numerical stability; the reinitialization is needed to keep the level set function a signed distance function with the property that the norm of the gradient of the level set function is as close to 1 as possible (within numerical errors) [26]. In current work, the reinitialization is introduced according to Olsson et al. [14,15] since the Level Set toolbox in Comsol Multiphysics is used. During the solution, the region boundaries are represented by the $\varphi = 0.5$ level set value. The equation provided by Olsson et al. [14,15] describes the evolution of the level set field depending on the velocity vector $\boldsymbol{u}$:

$$\frac{\partial \phi}{\partial \tau} + \overrightarrow{u} \cdot \nabla \phi = \gamma \nabla \cdot \left( \varepsilon_{\text{ls}} \nabla \phi - \phi(1 - \phi) \frac{\nabla \phi}{|\nabla \phi|} \right) \qquad (14)$$

Here, $\boldsymbol{u} = \boldsymbol{u}(x,y)$ is the velocity of the level-set surface. To solve the optimization problem, the normal velocity is needed. By using the normal vector $\boldsymbol{n}$ and normal velocity $V_n$ of the surface, the velocity $\boldsymbol{u}$ can be expressed as $\overrightarrow{u} = V_n \cdot \overrightarrow{n} = V_n \cdot (\nabla \phi / |\nabla \phi|)$.

As a result the $\overrightarrow{u} \cdot \nabla \phi$ term can be replaced with the relation:

$$\overrightarrow{u} \cdot \nabla \phi = V_n \frac{\nabla \phi}{|\nabla \phi|} \cdot \nabla \phi = V_n \frac{|\nabla \phi|^2}{|\nabla \phi|} = V_n |\nabla \phi| \qquad (15)$$

leading to the following equation to be solved:

$$\frac{\partial \phi}{\partial \tau} + V_n |\nabla \phi| = \gamma \nabla \cdot \left( \varepsilon_{\text{ls}} \nabla \phi - \phi(1 - \phi) \frac{\nabla \phi}{|\nabla \phi|} \right). \qquad (16)$$

In equation (16), the left hand side describes the movement of the level set surface while the right hand side guarantees numerical stability.

### 2.5. Battery materials and model

In the current study, a $LiPF_6 \cdot PEO_{20}$ polyethylene oxide electrolyte equivalent to 1.5 M $LiPF_6$ is simulated. The battery electrode

materials are LiCoO$_2$ (positive electrode) and graphite (negative electrode).

In the calculations, a 3D-MB trench geometry is simulated (Fig. 2a) consisting of planar Cu current collectors bases with attached perpendicular Al current collector plates, both coated with electrode materials. The trench geometry it is one of the most promising 3D-MB geometries [3] and can be considered a first step toward studying geometrically more complex 3D-geometries. In the current work, the battery simulation follows well established and experimentally validated electrochemical descriptions [18–24]. Material properties such as diffusion coefficients and conductivities of the electrodes and electrolytes are expressed by the level-set function, making it possible to describe changes in the electrode shape during the optimization. During the optimization process, the battery is simulated at steady-state, so that the material balance in the electrodes does not need to be taken into account. The Nernst–Planck equation is used to model the mass and current transport in the electrolyte, since previous studies [18] have demonstrated excellent agreement between experimental and simulation results at constant current. Furthermore, the Nernst–Planck equation is more convenient to use than concentrated solution theory based models [19–24] during the optimization routine described above, since it is computationally less expensive and more robust [27].

When the material boundary, expressed by the zero level set of the level set function, moves through the mesh elements, it is then possible to use only homogeneous Neumann boundary conditions or continuity boundary conditions for both electrical current and ionic flux at the electrode–electrolyte interface, since the material boundary is generally not conforming with the mesh element edges. In order to use previously validated battery models [18–24], porous electrodes must be implemented, since homogeneous Neumann boundary conditions then can be applied at the electrode–electrolyte interfaces. The use of porous electrodes is also advantageous since random numerical errors may occur when the material boundaries move through the elements, which can stop the optimization iterations prematurely [13]. These random errors are smoothed out when utilizing porous electrodes.

To perform the calculations, the diffusion coefficients and conductivities must be expressed through the level set function. Consequently, the conductivity of the electrolyte is

$$\sigma_l(\phi) = \varepsilon^{1.5}\sigma_l \cdot H(\phi) + \sigma_l \cdot (1 - H(\phi)),\qquad(17)$$

where the first term in the right side represents the conductivity of electrolyte inside the porous electrode material and the second term the conductivity of pure electrolyte. The conductivity in the electrodes is

$$\sigma_s(\phi) = (1 - \varepsilon)^{1.5}\sigma_j \cdot H(\phi) + \sigma_0 \cdot (1 - H(\phi)), \quad j = \mathrm{n, p}\qquad(18)$$

where $j = n$ corresponds to positive electrode and $j = p$ corresponds to negative electrode. $\sigma_0$ is an artificial parameter of very small value, introduced to avoid numerical singularities [9]. Finally, the diffusion coefficients in the electrolyte are formulated by:

$$D_i(\phi) = \varepsilon^{1.5}D_i \cdot H(\phi) + D_i \cdot (1 - H(\phi)), \quad i = \mathrm{Li, PF_6},\qquad(19)$$

The Butler–Volmer equation describes the charge transport between the electrode and electrolyte:

$$j = i_0\left[\exp\left(\frac{\alpha_a F\eta}{RT}\right) - \exp\left(-\frac{\alpha_c F\eta}{RT}\right)\right]\qquad(20)$$

where $\eta = \varphi_s - \varphi_l - V_{oc}$. The open circuit potential is fitted to experimental data according to Ref. [28]. Since the electrode reactions in Li batteries are fast and usually limited by mass transport, a high constant exchange current density ($i_0 = 100$ A m$^{-2}$) is used during the optimization to avoid numerical errors which may arise at the electrode–electrolyte boundary, expressed by the level-set function. During the time dependent simulations of the discharge processes, the exchange current density is calculated as $i_0 = F(k_a)^{\alpha_c}(k_c)^{\alpha_c}(c_{s,max}^j - c_s^j)^{\alpha_c}(c_s^j)^{\alpha_c}(c)^{\alpha_a}$, where $j = n,p$, $k = k_a = k_c = 2 \cdot 10^{-11}$ m s$^{-1}$ and $\alpha_a = \alpha_c = 0.5$ in order to achieve an initial exchange current density close to values reported in literature [23,24].
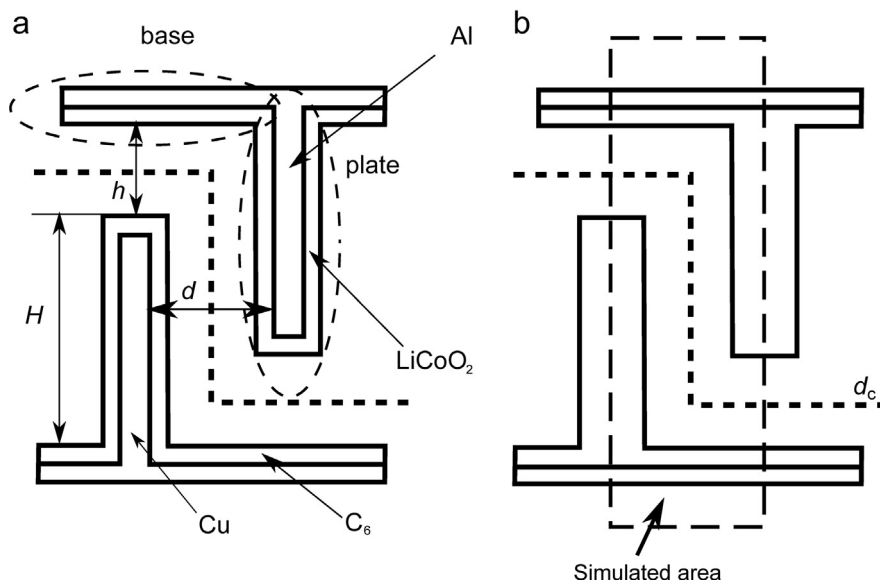


**Fig. 2.** Geometry of the 3D-trench model and electrode plate arrangement in 3D-trench geometry; (a) represents the geometry of the optimization problem and (b) the geometry of the test problem.

When optimizing the electrode shape, the flux of specie $i$ obeys the Nernst–Planck equation [29]:

$$J_i = -D_i(\phi)\nabla c_i - \frac{z_i F}{RT} D_i(\phi) c_i \nabla \phi, \quad i = \text{Li}, \text{PF}_6 \tag{21}$$

where $c_i$ is the concentration, $D_i$ the diffusion coefficients of species $i$, $z_i$ the charge number, $F$ Faraday's constant, $R$ the universal gas constant and $\varphi$ the potential in electrolyte. Electro-neutrality in the electrolyte is assumed, so that $c = c_{\text{Li}} = c_{\text{PF}_6}$.

The concentration profile at steady state can then described according to Ref. [18], however, since the porous electrodes are used, the Li insertion is described by using the source term [24,30]:

$$\frac{2D_{\text{Li}}(\phi)D_{\text{PF}_6}(\phi)}{(D_{\text{Li}}(\phi) + D_{\text{PF}_6}(\phi))}\nabla^2 c = \frac{1 - t_+^0}{F} a_s j \tag{22}$$

The initial value of the concentration ($c_0$) is specified in Table 1. Since Li$^+$ ions can be inserted or removed from the electrolyte only by the electrode reactions, the boundary condition for Eq. (10) is [18]:

$$\frac{2D_{\text{Li}}(\phi)D_{\text{PF}_6}(\phi)}{(D_{\text{Li}}(\phi) + D_{\text{PF}_6}(\phi))}\overrightarrow{n}\cdot\nabla c = 0 \tag{23}$$

The steady-state solution of Eq. (10) requires an extra constraint to guarantee a unique solution. This is achieved by specifying the conservation of mass as [7]:

**Table 1**
Parameters used in the simulations.

| Symbol | Quantity | Value |
|--------|----------|-------|
| $D_{\text{Li}}$ | Diffusion constant for Li$^+$ ions in polymer electrolyte [33] | $2.5\cdot10^{-13}$ m$^2$ s$^{-1}$ |
| $D_{\text{PF}_6}$ | Diffusion constant for PF$_6^-$ ions in polymer electrolyte [33] | $3\cdot10^{-13}$ m$^2$ s$^{-1}$ |
| $D$ | Li diffusion constant in the active material [34] | $2.5\cdot10^{-13}$ m$^2$ s$^{-1}$ |
| $\sigma_{\text{Al}}$ | Electronic conductivity of positive current collector (Al) [25] | $3.75\cdot10^7$ S m$^{-1}$ |
| $\sigma_{\text{p}}$ | Electronic conductivity of positive electrode active material (LiCoO$_2$) [34] | $1\cdot10^{-2}$ S m$^{-1}$ |
| $\sigma_{\text{n}}$ | Electronic conductivity of negative electrode (LiC$_6$) [34] | 1 S m$^{-1}$ |
| $\sigma_{\text{Cu}}$ | Electronic conductivity of negative current collector (Cu) [25] | $5.95\cdot10^7$ S m$^{-1}$ |
| $c_0$ | Salt concentration in electrolyte [7] | 1.5 M |
| $j_0$ | Discharging current during optimization | 10 A m$^{-2}$ |
| $\varepsilon$ | Porosity of the electrodes | 0.5 |
| $i_0$ | Exchange current density during optimization | 100 A m$^{-2}$ |
| $k$ | Rate coefficient during discharging simulations | $2\cdot10^{-11}$ m s$^{-1}$ |
| $c_{s,\text{max}}^{\text{p}}$ | Maximum Li concentration in the active material of the positive electrode | 51,656 mol m$^{-3}$ |
| $c_{s,\text{max}}^{\text{n}}$ | Maximum Li concentration in the active material of the negative electrode | 28,225 mol m$^{-3}$ |
| $H$ | Height of the plate | $40\cdot10^{-6}$ m |
| $h$ | Distance between plate tip an opposing electrode base | $15\cdot10^{-6}$ m |
| $d$ | Distance between current collector plates | $15\cdot10^{-6}$ m |
| $d_c$ | Thickness of the level-set function separating layer | $1\cdot10^{-6}$ m |
| $\varepsilon_{\text{ls}}$ | Parameter controlling electrode–electrolyte interface thickness during optimization (during validation) | $0.5\cdot10^{-6}$ m ($1\cdot10^{-6}$ m) |
| $\gamma$ | Reinitialization parameter during optimization (during validation). | 100 m s$^{-1}$ (40 m s$^{-1}$) |

$$\frac{1}{V}\left(\int\limits_{\Omega} c\,\mathrm{d}\Omega - \int\limits_{\Omega} c_0\,\mathrm{d}\Omega\right) = 0 \tag{24}$$

Here, $\Omega$ is the electrolyte region, $V$ the volume of the electrolyte and $c_0$ the initial concentration.

During the optimization, the state of charge is kept constant. Moreover, the Li concentration in the electrodes is uniform, and it is assumed that the positive electrode is almost completely lithiated ($c_s = c_{s,\text{max}}^{\text{p}} - 1000$ mol m$^{-3}$) and negative almost completely delithiated ($c_s = 1000$ mol m$^{-3}$), corresponding to a discharged cell. This discharged cell is used since the result will guarantee uniform material utilization.

The potential in the electrolyte is calculated according to Refs. [7,27,29], since the porous electrodes are used, reaction current is specified by the source term [24,30]:

$$(D_{\text{PF}_6}(\phi) - D_{\text{Li}}(\phi))F\nabla^2 c - \nabla\cdot\left[\frac{F^2 c}{RT}(D_{\text{PF}_6}(\phi) + D_{\text{Li}}(\phi))\nabla\varphi\right] = a_s j \tag{25}$$

$$\overrightarrow{n}\cdot\left[(D_{\text{PF}_6}(\phi) - D_{\text{Li}}(\phi))F\nabla c - \frac{F^2 c}{RT}(D_{\text{PF}_6}(\phi) + D_{\text{Li}}(\phi))\nabla\varphi\right] = 0 \tag{26}$$

where $a_s$ is the specific surface area of the electrodes and is calculated as $a_s = 3\varepsilon/r_p$, where $r_p$ is radius of an active material particle. The current densities in the electrodes and in the current collectors are calculated by:

$$\nabla\cdot\sigma_i(\phi)\nabla\varphi = a_s j, \quad i = \text{Al}, \text{p}, \text{n}, \text{Cu} \tag{27}$$

$$\overrightarrow{n}\cdot(\sigma_{\text{Al}}(\phi)\nabla\varphi) = j_0 \tag{28}$$

$$\varphi|_{\text{negative\_current\_collector}} = 0, \tag{29}$$

where $\varphi$ is the electrode potential, $j_0$ is the discharging current in the current collector of the positive electrode and $\sigma_i$ is the conductivity. The values of coefficient $i$ represent the positive current collector ($i = \text{Al}$), the positive active material ($i = \text{p}$), the negative active material ($i = \text{n}$) and the negative current collector ($i = \text{Cu}$).

### 2.6. Cell performance evaluation

To evaluate the performance of the cell, the dissipated energy during the discharge process is calculated. First, the overpotential of the cell is defined as:

$$\Delta V = V_{\text{disc}} - V_{\text{OC}} \tag{30}$$

where $V_{\text{disc}}$ is the discharging voltage and $V_{\text{oc}}$ is the open circuit voltage of the cell, calculated as $V_{\text{oc}} = V_{\text{LiCoO}_2}(x_{\text{p}}) - V_{\text{LiC}_6}(x_{\text{n}})$, where $x_{\text{p}}$ is $x$ in Li$_x$CoO$_2$ and $x_{\text{n}}$ is $x$ in Li$_x$C$_6$ [28]. A zero overpotential represents the case where no net current is moving through the cell, while any non-zero overpotential value represents the energy required to operate the cell at a specific current.

According to Bard [29], the cell resistance can be calculated as:

$$r = \Delta V/j_0, \tag{31}$$

where $J$ is the discharge current density and $r$ is the combined charge and mass transport resistances. The use of current density, instead of current, results in a normalized resistance $r$ ($\Omega$ m$^2$). However, a numerical value of the resistance can be calculated by

multiplying the normalized resistance with the surface area of the current collector (i.e., the cell fingerprint area). We here define the cell performance (resulting from the cell geometry optimization) as the ratio of dissipated energy during discharge in the reference cell and in the optimized cell. The dissipated power is calculated by Joule–Lenz law, and therefore the performance increase is:

$$\frac{P_{nonopt}}{P_{opt}} = \frac{j_0^2 \cdot r_{nonopt}}{j_0^2 \cdot r_{opt}} = \frac{r_{nonopt}}{r_{opt}} \tag{32}$$

where $r_{nonopt}$ is the resistance in the reference cell, $r_{opt}$ is the resistance in the optimized cell and $j_0$ is the discharge current density. The performance increase characterizes the increase in the battery power, since the volume of the electrodes (battery capacity) is not changing during the optimization while the cell resistance is decreased.

### 2.7. Simulation setup

#### 2.7.1. Validation of the optimization algorithm

To validate the optimization routine, a suitable test problem with known optimal solution was solved. The most uniform current density in an electrochemical cell would be achieved in a conventional 2D-cell (however, with limited energy storage capability) with planar electrodes having equal surface area. In the test problem, the initial 3D-MB architecture uses flat current collectors, as illustrated in Fig. 2b. The simulation was carried out in the area between the dashed lines, while the symmetry of the structure was used to extend the result to the entire battery cell. Since the electrode and electrolyte spatial distribution are described by the level-set function (Eqs. (1)–(3) and Fig. 1) and the level-set function value 1 corresponds to the electrode, the level-set function was required to be 1 in the current collectors to ensure that at least some amount of the electrode material is always attached to them (Eq. (18)). The optimization algorithm would then converge when the electrode geometry becomes 2-dimensional, since a homogeneous current density is achieved.

In the calculations, the geometry was discretized using ∼ 15,000 triangular linear elements.

#### 2.7.2. Optimization of the 3D-trench geometry and evaluation of the results

The optimization of the electrode shape was carried out using the geometry represented in Fig. 2a. At the start of the optimization procedure, the current collectors were coated with a uniform layer of electrode materials while the level set function value in the electrodes and the electrolyte was 1 and 0, respectively, so that the electrode–electrolyte boundary was represented by a 0.5 value. During the optimization, the shape of both electrodes was changed. However, since one "optimal" configurations is achieved when the electrodes are connected (representing a short-circuited cell), a thin separating region ($d_c$ in Fig. 2) where the level set function was required to be 0 was introduced. The electrode boundary can thereby not move over this region during the optimization process. All material properties and geometrical parameters are specified in Table 1. During the optimization, a current density of 10 A m$^{-2}$ was used.

In the calculations, a triangular mesh with ∼ 48,000 linear elements was used. A high number of elements were required to accurately model the battery regions where thin electrode material layers were developing.

After the optimization procedure was finished, the effects of the optimization of the battery geometry was evaluated by full cell charge/discharge simulations and compared to the pre-optimized 3D-trench model. Time dependent charge/discharge simulations were carried out with the optimized geometry and compared to simulations of a reference scenario. The reference scenario was the starting point of the optimization — i.e., the 3D-trench architecture with uniform electrode thickness. The effect of the optimization was evaluated by discharging fully charged cell; the current densities used for evaluation in both optimized and reference geometries were either 2 A m$^{-2}$, 4 A m$^{-2}$, 6 A m$^{-2}$, 8 A m$^{-2}$ or 10 A m$^{-2}$. For the evaluation of the optimization results, new geometrical model of the optimized battery geometry was constructed, so that the electrodes were modeled geometrically, independently from the level-set function.

In the calculations, a triangular mesh of ∼ 2700 linear elements was used to simulate the optimized geometry. For the reference geometry, ∼ 1700 triangular quadratic elements were used.

For the time dependent charging–discharging simulations, the Battery toolbox in Comsol Multiphysics 4.2 [25], utilizing concentrated solution theory [19–24] was used.

## 3. Results and discussion

### 3.1. The test problem

The progression of the solution of the test problem described in paragraph 2.7.1 is presented in Fig. 3. Black color represents the
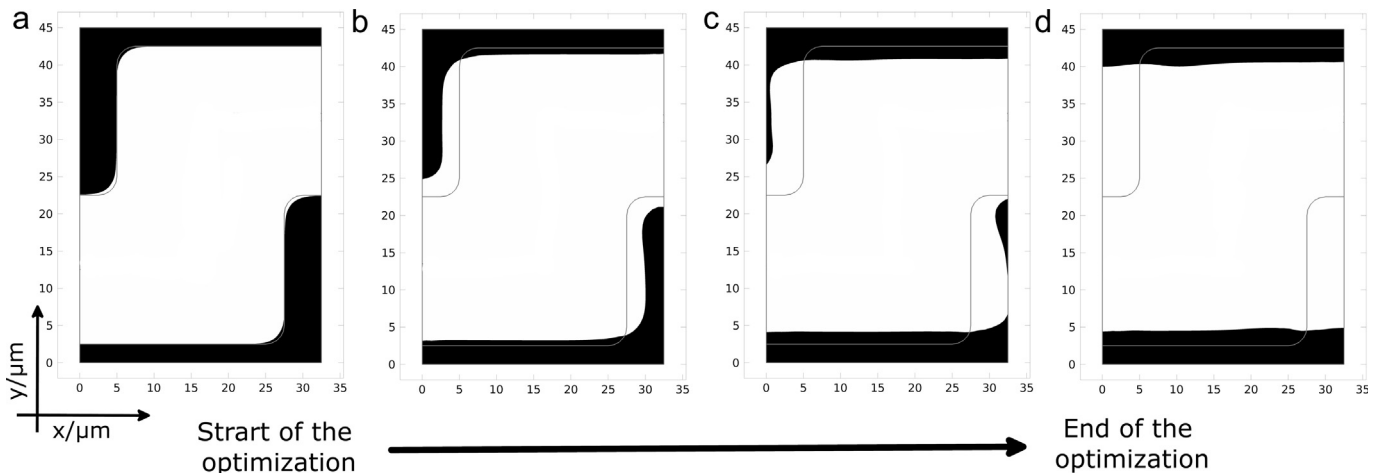


**Fig. 3.** Electrode shape development for the optimization test problem during the calculation (a–d). Black color represents electrode material and white color the electrolyte. During the optimization, the 3D-electrode geometry (a) is transformed to a 2D-electrode (d).

electrodes and white represents the electrolyte; both electrodes have a constant volume during the optimization. It is clearly seen how the optimization routine starts to remove material from the electrode plates and increase the thickness of the electrode base. As expected, the plates are removed during the course of the optimization and the material is carried over to the base of the electrode, forming planar electrodes with only negligible distortions. The solution of the test problem clearly demonstrates the expected behavior of the optimization algorithm for this multiphysics problem.

## 3.2. Optimization of the 3D-trench geometry

The results of the optimization of the electrode material distribution in the 3D-trench geometry are presented in Fig. 4. Again, black represents the electrode and white the electrolyte area. As opposed to the test problem, fixed 3D-structured current collector substrates are coated with electrode materials (see Fig. 2a), thereby reassuring a 3D-MB as the optimization result. The optimization routine progresses toward a homogeneous current density (by minimizing the objective function). At the beginning of the optimization process, the current density is very high at the tips of the electrodes and low at the electrode base. To obtain the most uniform current density, the optimization routine starts to rearrange the active material so that the electrode areas with high current density gain more material, resulting in increased local surface area and decreased local current density (due to that the material amount increase in the electrode tips). Alternatively, by surrounding certain parts of the electrodes with a larger mass of electrolyte higher local resistivity values are achieved (the amount of material decreases at the electrode base). This process continues gradually during the whole optimization cycle and finally creates electrodes where almost all active material has been transferred from the bottom of the electrodes to the tips.

The optimal distribution of material is different for the positive and negative electrode. During the optimization, most material on the positive electrode is assembled at the tip of the plate and only a small amount is left at the base of the electrode. The optimal shape of the negative electrode is more complex. At the beginning of the optimization, the evolution of both electrode shapes is similar, but after $\sim$50% of the calculation is finished, a sharp corner starts to develop at the tip of the electrode. Moreover, the optimization routine starts to move material from the center of the tip of the negative electrode (Fig. 4c). As a result, the local surface area of the electrode tip is increasing and local current density decreases.

The explanation for this behavior is that since one of the optimal electrode configurations is achieved when the positive and negative electrodes are connected (which represents a short-circuited cell), a thin region $d_c$ (Fig. 2) has been created between the electrodes, dividing the electrolyte into two volumetrically equal parts. While the optimization of the positive electrode is unaffected by this constraint, it influences the shape of the negative electrode at the end of the calculation by creating a negative electrode with sharp corners (Fig. 4d). In future studies, the model could be improved by addition of moving mesh interfaces, making it possible to move the separating region away from the surface of the optimized electrode. This would also allow optimization of electrodes with very short separating distances.

During the optimization, both electrodes lose $\sim$10% of their volume. This loss of material is caused by the Lagrange multiplier, presented in Eqs. (12) and (13) since the total volume of the material is not mathematically represented when using the derivative (Eq. (12)). The Lagrange multiplier instead enforces zero material change. However, small numerical errors will always occur during the iterative computer simulations which gradually can allow the system to deviate from its initial volume. Such a small violation of the volume constraint is often reported in literature [12,13] discussing optimization with the level set method. However, the impact on the results should be limited since it is easily identified as
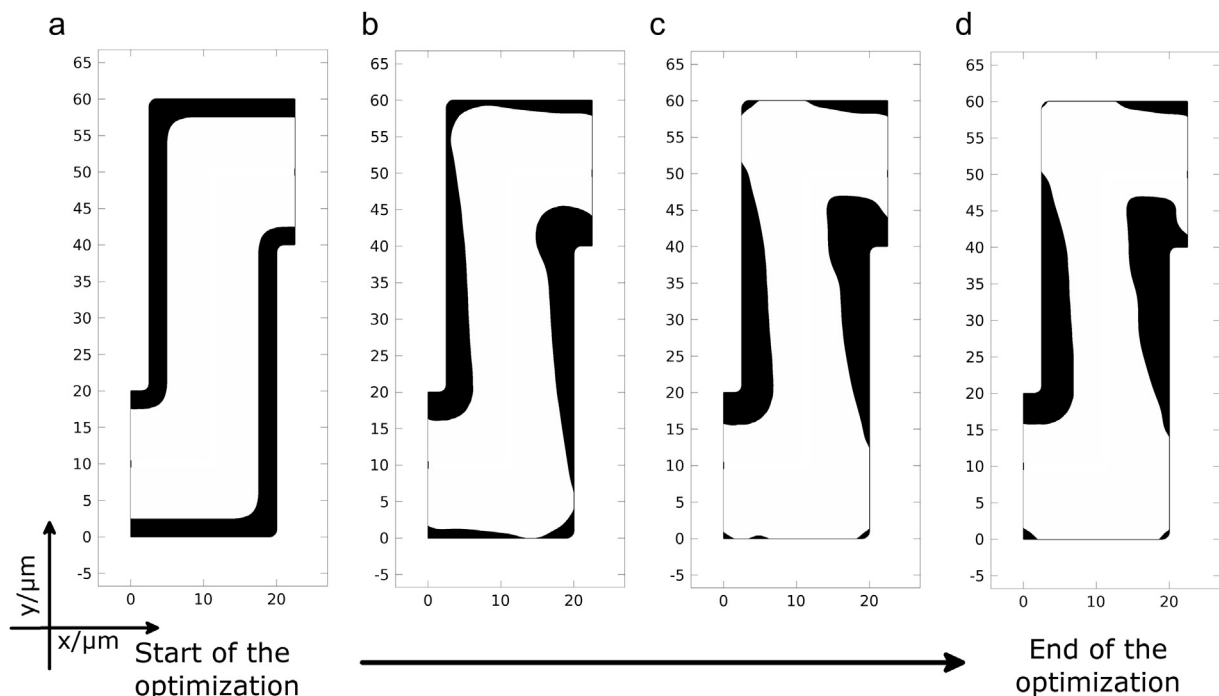


Fig. 4. Evolution of the electrode shape during the optimization procedure. The uniform material coating (a) is transformed and the electrode material is rearranged (d). Black represents the porous electrode materials; white electrolyte.

a systematic error in all comparisons and the results, comparing the discharge curves and performance are plotted in normalized scale.

Although there exists a wide range of proposed 3D-MB geometries, the "trench" geometry has been the focus of the current studies. Other 3D-geometries such as pillar architectures in interdigitated or concentric arrangements [1] would also be important to study as good candidates for 3D-MBs. However, the trench geometry is one of possible 3D-MB geometries closest to realization, and it can also be considered as a model for the interdigitated and concentric geometries. For example, if the simulated trench geometry is rotated, a concentric geometry is obtained, or if the electrodes in the current geometry are rotated, an interdigitated pillar geometry is achieved. Due to symmetry considerations, the current density distribution in the interdigitated design would probably be somewhat less uniform than in the trench geometry, since the current density distribution will change also around the pillar cross-sections [4,6]. An optimization should therefore lead to a similar electrode material distribution as presented here, but with a slight material layer thickness variation around the pillar cross-section.

### 3.3. Performance of the optimized cell

The current density distributions in the optimized and reference (starting) 3D-MB geometries are presented in Fig. 5 during the discharge of the cell for a current of 10 A m$^{-2}$. The current density distribution in the reference geometry demonstrates a significant development during the course of the discharge. At the beginning of the process, at $t = 0$ s, the current density is maximal at the tip of the positive electrode and most of the current is moving between electrode plates. As the simulation progresses (at $t = 350$ s; Fig. 5e), the current density maximum moves to the negative electrode, similarly as for liquid electrolytes in the same geometry [6]. At the same time, the ionic transport pathways (represented by current density streamlines) are becoming longer, since the electrode material at the tips is being depleted due to higher activity in these regions. Mass and charge transport continues through the electrode bases, resulting in longer transport distances, and thereby higher cell resistance. At the end of the discharge (at $t = 700$ s; Fig. 4f) the maximum current density can still be found at the negative electrode, but now the current moves almost completely
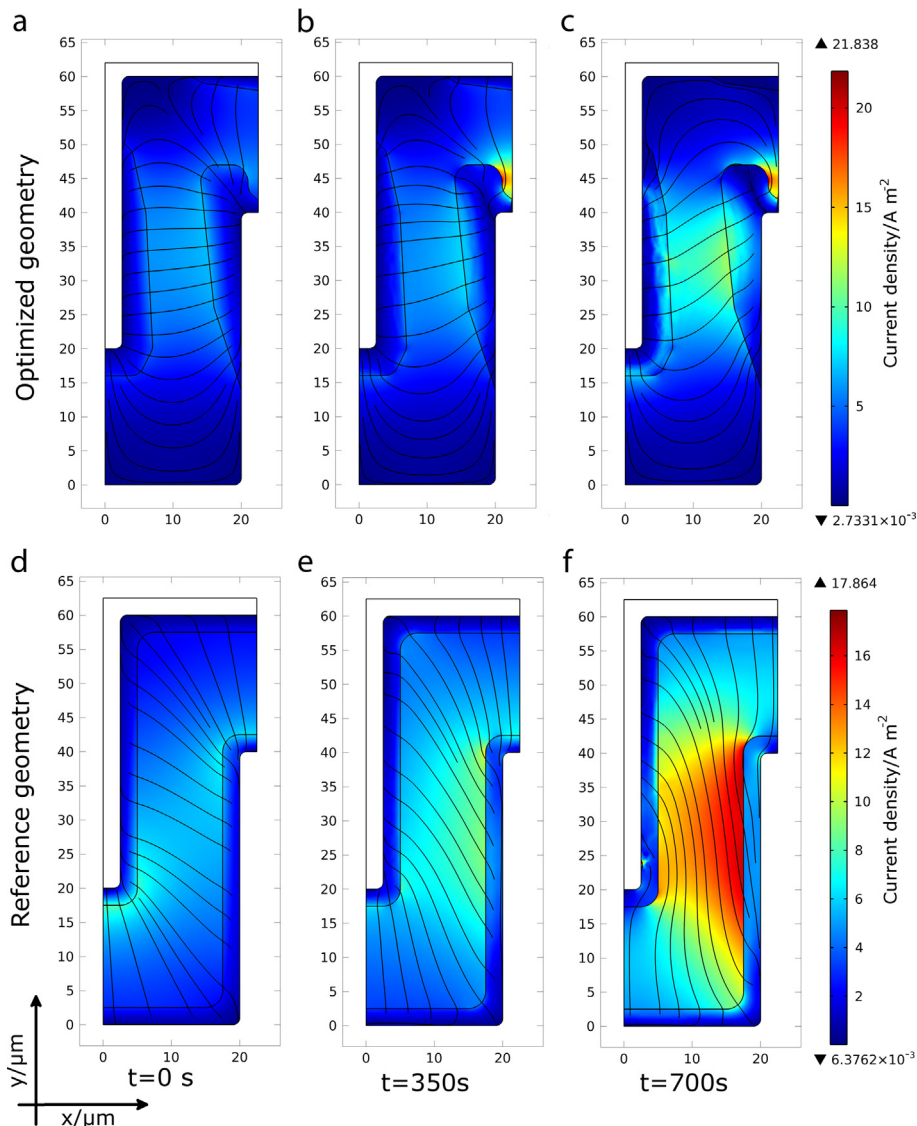


**Fig. 5.** Current density distribution in the electrolyte of the optimized (a–c) and reference (d–f) 3D-MB geometries. The streamline density is uniform and does therefore not represent the current density magnitude.

between electrode bases. The ionic transport pathways and cell resistance are significantly increased and the ions must travel up to 60 μm to reach the opposite electrode, instead of 10−20 μm at the beginning of the discharge. Thus, the energy lost due to the transport of the ions is increased. To balance this effect in the non-optimized cell, the ionic conductivity of the electrolyte has to be much higher.

The optimized geometry, on the other hand, displays much less time dependent changes in the current density distribution. It can be seen in Fig. 5a−c how the current density distribution remains almost unchanged through the simulated discharge process − the changes are very small and appear at the end of the discharge. The most significant changes appear at the tip of the negative electrode, and are visible in Fig. 5b and c where a significant increase in the current density (as compared to Fig. 5a) is seen. This increase of current density is caused by the locally limited electrolyte volume electrochemically associated with a large electrode surface area. On the other hand, this "hole" at the tip of the electrode, constructed by the optimization procedure, makes it possible to discharge this rather large part of the electrode uniformly.

The current density in the optimized geometry is dominated by the electrode plates, which is expected, considering that much

material from the bottom of the electrodes has been removed during the optimization procedure. However, this re-arrangement of active material obviously makes it possible to achieve a much more uniform current density over the whole active material region.

The effects of the optimization can also be seen in Fig. 6, where the concentration distribution in the electrodes is presented. It can be seen that the Li concentration in the active material in the optimized electrodes changes uniformly during discharge − the concentration distribution in almost all parts of the electrode changes with equal speed. In contrast, the reference geometry shows significant changes in Li concentration in the electrodes; the charging/discharging starts from the plate tips and progresses through the whole electrode plate toward the base, which is charged/discharged last. This kind of charging/discharging dynamics increases the local current densities (as seen in Fig. 5) and creates extra stress in the material due to non-homogeneous volume changes in the electrodes, leading to shorter cell lifetime.

The cell voltage as a function of the amount of Li in the positive electrode is presented in Fig. 7, where simulation results for a range of discharge currents are presented. The dashed lines represent the reference geometry, while the solid lines represent the optimized
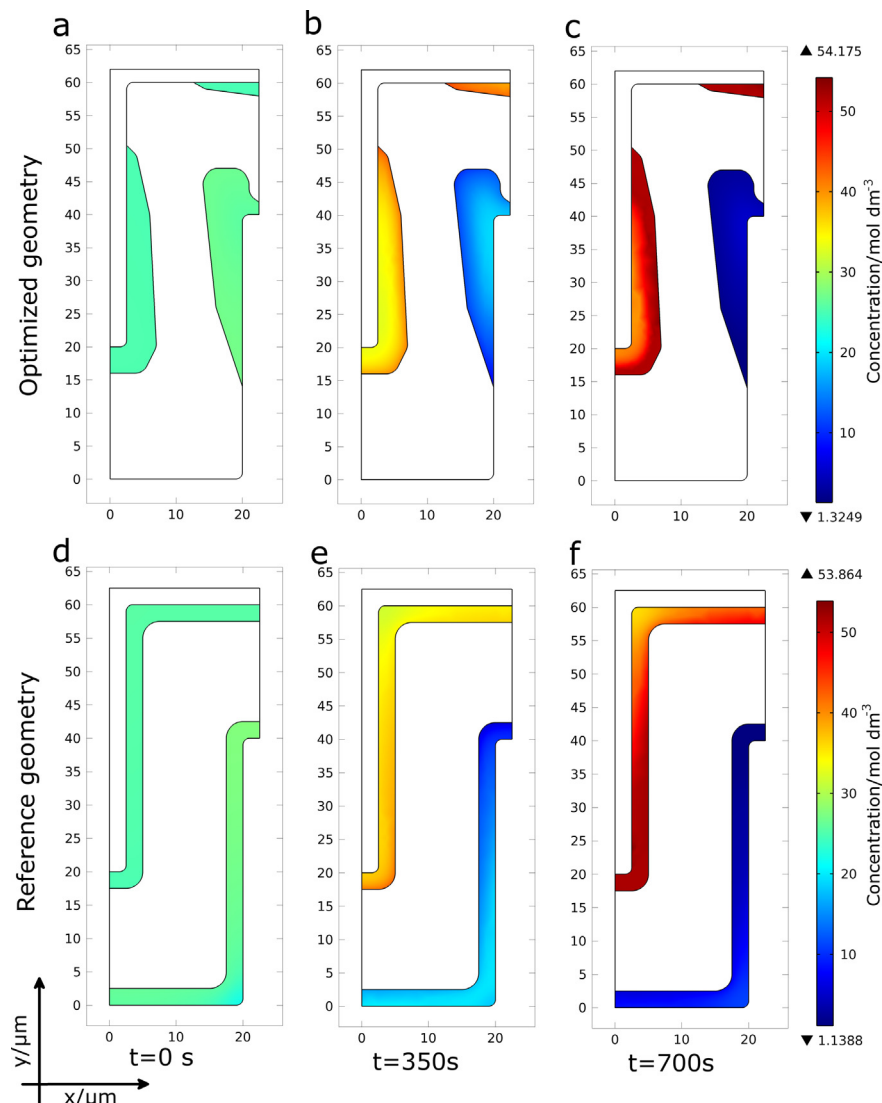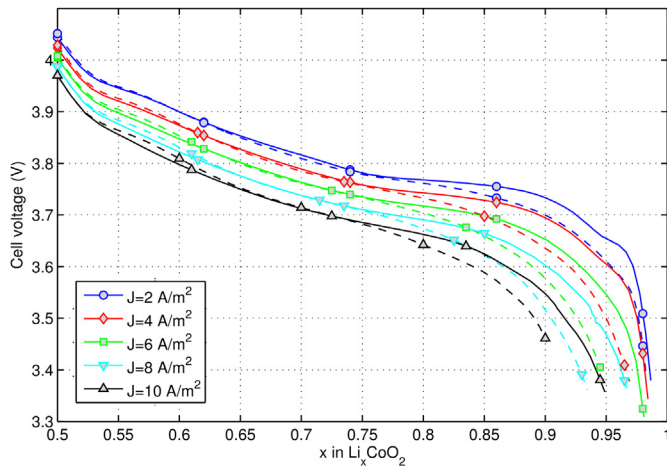


**Fig. 6.** Concentration distribution in the electrodes of optimized (a−c) and reference (d−f) 3D-MB geometries.

**Fig. 7.** Discharge curves of the cells with optimized and non-optimized 3D-MB geometries for different current values. Dashed lines represent the reference geometry and solid lines the optimized geometry.

geometry. It is seen that the optimized and reference geometry provide very similar result at the beginning of the discharge. However, when the lithiation of $Li_xCoO_2$ progress beyond $x = 0.75$, the performance of the reference cell drops. This has vital influences on the battery performance. For example, the discharge curves for the optimized geometry at 4 A m$^{-2}$ and the non-optimized at 2 A m$^{-2}$ discharge current density, more or less overlap for $x > 0.85$. This means that the optimized geometry can provide twice as high current for the same voltage, thus significantly increasing the power of the battery.

Generally, the discharge curves for the optimized geometry remain at a higher voltage for a longer time due to the unchanged current density distribution in cell (Fig. 5), leading to uniform charging/discharging of the electrode materials (Figs. 5 and 6). In the reference geometry, on the other hand, the active material in the plates is depleted first, followed by the use of active material in the electrode bases. As a result, the discharge curves of the optimized and reference cell coincide during the first half of the discharge ($x < 0.75$), since the ion transport distances are similar. However, the ionic transport pathways and cell resistance increase when the charge and mass transport in the 3D-cell start to proceed mainly through electrode bases in the second half of the discharge

cycle ($x > 0.75$), resulting in a cell voltage drop. Similar trends can be seen also for other discharge curves.

In Fig. 8, the overpotential and resistance of the cells are presented. The dashed line represents the reference (non-optimized) geometry and the solid line represents the optimized geometry. The overpotential (Fig. 8a) follows similar characteristics during all discharge currents, obtaining gradually higher values when the discharging current is increased. The overpotential in the optimized and reference geometries almost coincide for all currents for $x < 0.75$ in $Li_xCoO_2$. However, when $x$ increases above 0.75, the effects of the optimization become apparent. The overpotential required to operate the battery increases significantly for both the reference and optimized cell, but its increase is significantly lower for the optimized geometry. The overpotential tends to be slightly lower in the reference geometry at the beginning of discharge, when $x < 0.65$. This is due to that the optimal geometry is generated at steady-state conditions which are not yet fulfilled at the beginning of discharge.

The cell resistance is presented in Fig. 8b. During the first half of the discharge, while $x < 0.75$ in $Li_xCoO_2$, the resistance is almost independent of $x$ in $Li_xCoO_2$ and discharging current strength for both geometries. Moreover, the resistances are almost equal for both cases. However, when the discharge reaches the second half of the cycle, beyond $x = 0.75$, the resistance starts to increase fast for both geometries, corresponding to the increase in overpotential. The resistance in the reference geometry is almost independent of the current strength in the second half of the discharge cycle. In the optimized geometry, on the other hand, the resistance depends more strongly on the current, and is higher for higher current values. This can be explained by the active material layer thickness at the tips of the electrodes, which leads to a higher concentration overpotential in the electrolyte in the electrode pores at the end of the discharge when higher currents are used. However, this effect is small compared to the overall decrease of the overpotential due to the optimization.

The performance increase (defined in 2.6) due to geometry optimization is presented in Fig. 9. Dashed lines represent individual performance increases for different discharging currents and solid line represents average performance increase. The data show the amount of additional energy needed in the reference cell (non-optimized geometry) as compared to the optimized cell to maintain a specific current. The performance of the optimized cell tends to be slightly lower than the performance of the reference cell at the beginning of the discharge, being most apparent for $J = 2$ A m$^{-2}$. However, for other current values, the performance increase is
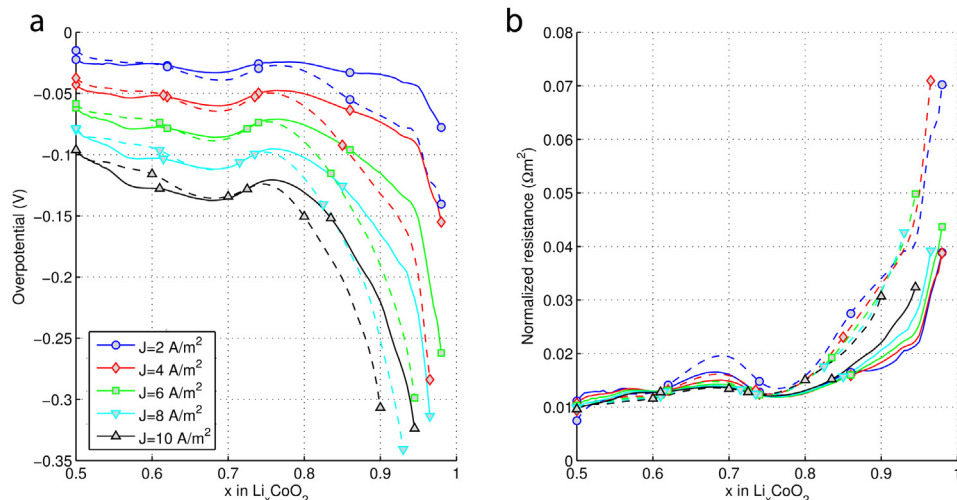


**Fig. 8.** Overpotential (a) and normalized cell resistance (b) for different discharge currents for optimized (solid lines) and non-optimized (dashed lines) geometries.
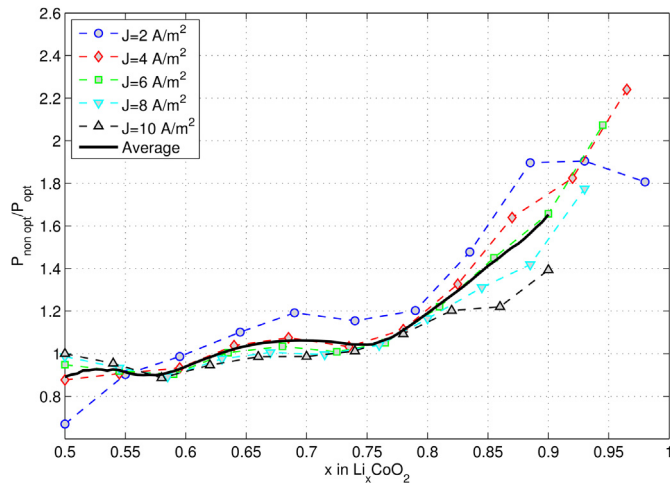
**Fig. 9.** Performance increase in the optimized cell as compared to the reference cell during discharge.

almost the same, being around 0.9. The average performance increase to above 1 at $x \approx 0.63$ and remains almost constant until $x = 0.75$. Within this range, the average performances of the optimized and non-optimized cells are approximately equal. However, when $x > 0.75$, the performance increases fast. The average performance increases from 1 to 1.65, indicating that the energy needed for the mass transport in the optimized cell is 65% smaller than in the reference cell. Moreover, at lower current densities ($J = 2$ A m$^{-2}$ and $J = 4$ A m$^{-2}$), the maximal performance increase is more than twice as high, reaching a maximum at 2.25 for $J = 4$ A m$^{-2}$. However, when the current density increases, the maximum performance increase is limited to 1.4 for $J = 10$ A m$^{-2}$. This performance loss at higher discharge currents for the optimized geometry is caused by the higher concentration overpotential in the porous electrodes, seen in Fig. 8a.

The optimized geometry can provide as much as twice as high current as the non-optimized one. The energy dissipated during the discharge in the cell is released as heat. Thus, up to two times less heat is released due to the optimization. This effect increases the safety of the cells by decreasing the probability of overheating and thermal runaway. The lifetime of the optimized cells will also increase, since less side reactions can occur. In the non-optimal geometry, a situation can occur where the local current density in certain parts of the electrode (such as the tips) becomes equal or higher than the limiting current. This will trigger side reactions which can destroy both electrode and electrolyte material, further reducing cell performance and ultimately destroying the cell.

It is important to address the question whether it is possible or not to construct this kind of complex non-uniformly coated electrode structure for 3D-MBs. In fact, some recent studies suggest that non-uniform coating can well be the result of many deposition techniques. For example, Lethien et al. [31] recently synthesized an interdigitated 3D-MB positive electrode of silicone nanopillars coated with layers of LiPON and LiFePO$_4$, resulting in a geometry similar to the one presented here: the pillars tips were considerably thicker than the rest of the electrode. Similar results were also seen in studies of Lafont et al. [32]. This indicates that the simulation results presented here might well be non-difficult to realize.

## 4. Conclusions

In this paper, a variation of the level set method is used for optimization of a novel type of a multiphysics problem, consisting of coupled diffusion and conductive media problems. The level set method is used to optimize the electrode shapes in a 3D-microbattery architecture. The optimized geometry was thereafter evaluated by carrying out discharge cycles for different current values. A comparison between the discharge simulations of optimized and reference geometry demonstrated that the optimization affects primarily the second half of the discharge, when $x > 0.75$ in Li$_x$CoO$_2$. The most significant effects on the battery voltage development occur during the last third of the discharge cycle, from $x > 0.85$ to $x = 1$. The optimized geometry demonstrates considerably better results; it is possible to reduce the energy dissipated due to charge and mass transport up to 2.25 times, while the average performance increase was up to 1.65 times. This is due to the fact that the concentration distribution in the optimized electrodes demonstrates a uniform lithiation/delithiation change over the whole electrode during discharge, while the reference cell electrodes were discharged non-uniformly. This clearly demonstrates that by tailoring the material deposition onto the substrates when constructing 3D-MBs, higher power and energy density can be achieved.

## References

[1] J.W. Long, B. Dunn, D.R. Rolison, H.S. White, Chem. Rev. 104 (2004) 4463.
[2] M. Roberts, P. Johns, J. Owen, D. Brandell, K. Edstrom, G.E. Enany, C. Guery, D. Golodnitsky, M. Lacey, C. Lecoeur, H. Mazor, E. Peled, E. Perre, M.M. Shaijumon, P. Simon, P.-L. Taberna, J. Mater. Chem. 21 (2011).
[3] J.F.M. Oudenhoven, L. Baggetto, P.H.L. Notten, Adv. Energy Mater. 1 (2011) 10.
[4] R.W. Hart, H.S. White, B. Dunn, D.R. Rolison, Electrochem. Commun. 5 (2003) 120.
[5] V. Zadin, D. Brandell, H. Kasemägi, A. Aabloo, J.O. Thomas, Solid State Ionics 192 (2011) 279.
[6] V. Zadin, H. Kasemägi, A. Aabloo, D. Brandell, J. Power Sources 195 (2010) 6218.
[7] V. Zadin, D. Brandell, Electrochim. Acta 57 (2011) 237.
[8] M.P. Bendsøe, O. Sigmund, Topology Optimization: Theory, Methods, and Applications, Springer, 2003.
[9] M.P. Bendsøe, Struct. Multidiscip. O. 1 (1989) 193.
[10] S.J. Osher, F. Santosa, J. Comput. Phys. 171 (2001) 272.
[11] M.Y. Wang, X. Wang, D. Guo, Comput. Meth. Appl. Mech. Eng. 192 (2003) 227.
[12] M.Y. Wang, X. Wang, Comput. Meth. Appl. Mech. Eng. 193 (2004) 469.
[13] Z. Liu, J.G. Korvink, R. Huang, Struct. Multidiscip. O. 29 (2005) 407.
[14] E. Olsson, G. Kreiss, J. Comput. Phys. 210 (2005) 225.
[15] E. Olsson, G. Kreiss, S. Zahedi, J. Comput. Phys. 225 (2007) 785.
[16] C. Zhuang, Z. Xiong, H. Ding, Comput. Meth. Appl. Mech. Eng. 196 (2007) 1074.
[17] Z. Luo, L. Tong, H. Ma, J. Comput. Phys. 228 (2009) 3173.
[18] D. Danilov, P.H.L. Notten, Electrochim. Acta 53 (2008) 5569.
[19] M. Doyle, J. Newman, A.S. Gozdz, C.N. Schmutz, J.-M. Tarascon, J. Electrochem. Soc. 143 (1996) 1890.
[20] P.M. Gomadam, J.W. Weidner, R.A. Dougal, R.E. White, J. Power Sources 110 (2002) 267.
[21] M. Doyle, T.F. Fuller, J. Newman, J. Electrochem. Soc. 140 (1993) 1526.
[22] J. Newman, K.E. Thomas, H. Hafezi, D.R. Wheeler, J. Power Sources 119–121 (2003) 838.
[23] Q. Zhang, Q. Guo, R.E. White, J. Power Sources 165 (2007) 427.
[24] T.F. Fuller, M. Doyle, J. Newman, J. Electrochem. Soc. 141 (1994) 1.
[25] http://www.comsol.com/.
[26] M. Sussman, P. Smereka, S. Osher, J. Comput. Phys. 114 (1994) 146.
[27] V. Zadin, D. Danilov, D. Brandell, P.H.L. Notten, A. Aabloo, Electrochim. Acta 65 (2012) 165.
[28] A.T. Stamps, S. Santhanagopalan, E.P. Gatzke, J. Electrochem. Soc. 154 (2007) P20.
[29] A.J. Bard, L.R. Faulkner, Electrochemical Methods: Fundamentals and Applications, second ed., Wiley, 2000.
[30] W. van Schalkwijk, B. Scrosati, Advances in Lithium-ion Batteries, first ed., Springer, 2002.
[31] C. Lethien, M. Zegaoui, P. Roussel, P. Tilmant, N. Rolland, P.A. Rolland, Microelectron. Eng. 88 (2011) 3172.
[32] U. Lafont, A. Anastasopol, E. Garcia-Tamayo, E. Kelder, Thin Solid Films 520 (2012) 3464.
[33] J. Karo, D. Brandell, Solid State Ionics 180 (2009) 1272.

[34] M. Park, X. Zhang, M. Chung, G.B. Less, A.M. Sastry, J. Power Sources 195 (2010) 7904.

## Nomenclature

$a$: specific area of an electrode (m$^{-1}$)
$c$: concentration (mol m$^{-3}$)
$D$: diffusion coefficient (m$^2$ s$^{-1}$)
$F$: Faraday constant (96,487 C mol$^{-1}$)
$H,h,d,d_c$: geometrical parameters of the cell (Table 1)
$i_0$: exchange current density (A m$^{-2}$)
$J$: ionic flux
$k$: rate constant (m s$^{-1}$)
$r$: normalized resistance of the cell ($\Omega$ m$^2$)
$R$: universal gas constant (8.314 J (mol K)$^{-1}$)
$T$: absolute temperature (K)
$V$: volume of the electrolyte (m$^3$)
$V_{oc}$: open circuit voltage (V)
$z$: charge number
$\vec{j}$: current density (A m$^{-2}$)
$t_+^0$: transference number of Li$^+$ ions in the electrolyte
$\vec{n}$: unit normal vector

*Greek letters*
$\phi$: the level-set function
$\alpha$: transfer coefficient
$\gamma$: reinitalization parameter (m s$^{-1}$)

$\delta(x)$: Dirac delta function
$\varepsilon$: porosity of the electrodes
$\varepsilon_{ls}$: electrode−electrolyte interface thickness during optimization (m)
$\eta$: surface overpotential in the battery (V)
$\lambda$: Lagrange multiplier (A m$^{-2}$)
$\sigma$: conductivity (S m$^{-1}$)
$\varphi$: electrical potential (V)
$\Omega$: geometrical region of the problem (m)
$\tau$: pseudo time, representing the optimization step

*Subscripts*
$Li$: Li$^+$ ions
$PF_6$: PF$_6^-$ ions
0: corresponding to constant initial value or boundary condition
$a$: anodic
$c$: cathodic
$i$: defined when used
$j$: defined when used
$l$: liquid phase (electrolyte)
$s$: solid phase (electrode material)
$opt$: optimized cell
$nonopt$: nonoptimized (reference) cell

*Superscripts*
$n$: positive electrode
$p$: negative electrode
$*$: electrodes